Control of Flow Past a Wing Section with Plasma-based Body Forces

Datta V. Gaitonde[*] & **Miguel R. Visbal**[†]

Computational Sciences Branch

Air Vehicles Directorate

Air Force Research Laboratory

Wright-Patterson AFB, OH 45433

Subrata Roy[‡]

Department of Mechanical Engineering

Kettering University

Flint, MI 48504

The response of the flow past a stalled NACA 0015 airfoil at $15\deg$ angle of attack and Reynolds number of $45,000$ to body forces originating from radio-frequency asymmetric dielectric-barrier-discharge actuators is described via direct numerical simulations. The theoretical model couples a phenomenologically derived averaged body force with a high-order 3-D compressible Navier-Stokes solver. The body force distribution is assumed to vary linearly, diminishing away from the surface until the critical electric field limit is reached. Various magnitudes and orientations of the force field are explored, ranging from vertically upwards (away from the body) to vertically downwards (towards the body). The imposed body forces couple to the non-linear inertial terms and the pressure gradients to engender a complex sequence of events. A significant streamwise component assures the reduction or elimination of stall with the formation of a stable wall-jet. When the only component of the force vector is pointed normal to and away from the surface, no control effect is achieved. On the other hand, when the force vector is directed towards the surface, a shallower separation region is observed, accompanied by unsteady boundary layer development. At the low Mach number considered (0.1), the work done by the force has little impact on the solution, and density variations remain less than 5%. Relaxation effects are explored by abruptly switching off the force, and estimates of response times are noted. The lack of a proper spanwise breakdown mechanism for the separated shear layer in 2-D simulations results in large coherent structures, whose response in transient and unsteady asymptotic states differ significantly from those observed in 3-D. Nonetheless, if the force is sufficiently effective to eliminate separation, the flowfield becomes generally two-dimensional and steady in the vicinity of the airfoil, and the overall results from 2-D and 3-D analyses yield similar results.

I.   Introduction

Plasma-based techniques exploiting electromagnetic forces for flow control are currently of considerable interest. Particularly attractive properties stem from the absence of moving parts and lack of mechanical inertia, which permits instantaneous deployment over a broad range of frequencies. Recent efforts have explored various possibilities both in high-speed[1,2] as well as low-speed applications.[3–5] The focus of this paper is on the latter speed regime, where striking experimental observations have been obtained with dielectric barrier discharge (DBD) based devices, which typically operate in the low radio frequency range of 1-10kHz and voltage amplitudes in the range of 5-10kV. A number of papers, including Refs. 5–7, have reported on the ability of such devices to inhibit separation over various airfoil sections, in both static as well as oscillating[8] situations. Recently, in Ref. 9, experiments at velocities up to $75\ m/s$ have been reported on a NACA 0015 airfoil, for which stall angle was increased from 15 to 21 degrees. The approach has also been effective in improving the flow in low-pressure turbine blade passages.[10–12] In Refs. 7, 11, 12, flow visualizations are complemented by detailed PIV measurements of the wall-jet structure. An overview of the basic concepts behind this control technique, including impact of duty cycle, may be found in Ref. 13.

Despite the significant recent progress, a clear understanding of the physics of operation is presently lacking. A framework for analysis was proposed in Ref. 3 by associating the phenomenology to the characteristics of the DBD,

---

[*]Tech. Area Leader, Associate Fellow AIAA
[†]Tech. Area Leader, Associate Fellow AIAA
[‡]Associate Professor, Associate Fellow AIAA.

Report Documentation Page		*Form Approved* *OMB No. 0704-0188*

Public reporting burden for the collection of information is estimated to average 1 hour per response, including the time for reviewing instructions, searching existing data sources, gathering and maintaining the data needed, and completing and reviewing the collection of information. Send comments regarding this burden estimate or any other aspect of this collection of information, including suggestions for reducing this burden, to Washington Headquarters Services, Directorate for Information Operations and Reports, 1215 Jefferson Davis Highway, Suite 1204, Arlington VA 22202-4302. Respondents should be aware that notwithstanding any other provision of law, no person shall be subject to a penalty for failing to comply with a collection of information if it does not display a currently valid OMB control number.

1. REPORT DATE **JUN 2005**	2. REPORT TYPE	3. DATES COVERED **00-00-2005 to 00-00-2005**
4. TITLE AND SUBTITLE **Control of Flow Past a Wing Section with Plasma-based Body Forces**		5a. CONTRACT NUMBER
		5b. GRANT NUMBER
		5c. PROGRAM ELEMENT NUMBER
6. AUTHOR(S)		5d. PROJECT NUMBER
		5e. TASK NUMBER
		5f. WORK UNIT NUMBER
7. PERFORMING ORGANIZATION NAME(S) AND ADDRESS(ES) **Air Force Research Laboratory,Computational Sciences Branch,Air Vehicles Directorate,Wright-Patterson AFB,OH,45433**		8. PERFORMING ORGANIZATION REPORT NUMBER
9. SPONSORING/MONITORING AGENCY NAME(S) AND ADDRESS(ES)		10. SPONSOR/MONITOR'S ACRONYM(S)
		11. SPONSOR/MONITOR'S REPORT NUMBER(S)
12. DISTRIBUTION/AVAILABILITY STATEMENT **Approved for public release; distribution unlimited**		
13. SUPPLEMENTARY NOTES		
14. ABSTRACT		
15. SUBJECT TERMS		

16. SECURITY CLASSIFICATION OF:			17. LIMITATION OF ABSTRACT **Same as Report (SAR)**	18. NUMBER OF PAGES **14**	19a. NAME OF RESPONSIBLE PERSON
a. REPORT **unclassified**	b. ABSTRACT **unclassified**	c. THIS PAGE **unclassified**			

Standard Form 298 (Rev. 8-98)
Prescribed by ANSI Std Z39-18

thus bringing to bear specific theories developed in plasma physics disciplines in non-aerospace contexts. Further diagnostic efforts have been reported in Ref. 14, which, based on acoustic measurements, concluded that compressibility effects may play a role in momentum coupling, though as noted in Ref. 13 there is little or no heating of the air.

Numerical modeling of high-Reynolds number flows with purely first-principles based approaches is a daunting endeavor. Quantitative aspects of many of the fundamental processes remain either unknown or computationally expensive. The is especially true for air – consequently most approaches treat simpler gases. Additionally, situations in which flow control is essential, such as stalled airfoils, are characterized by phenomena such as transition and turbulence, which also independently require massive simulation resources. These difficulties have fostered the development of a wide spectrum of models introducing varying degrees of empirical elements into the procedure. Among the simpler methods focused specifically on discharge-fluid coupling, are those of Roth[4] and Shyy et al.[15] Roth associated transfer of momentum from charged to neutral particles as effectively based on a gradient of electric pressure, which varies as the square of the electric field magnitude. This force varies as the product of the field and its gradient, which depends on the charge by Gauss' law. As pointed out in Ref. 3, this argument is strictly valid only in 1-D, where the electric field has only one component and may be treated as a scalar. A more sophisticated model, suitable for coupling with the fluid response was proposed by Shyy et al,[15] who developed separate estimates for the charge distribution and the electric field by coupling known plasma physics parameters to qualitative experimental data. Although the charge and electric field distribution are not consistent, the approach yields a simple force distribution varying linearly in both directions. In a further advance, Voikhov et al[16] describe several 2-D simulations with a consistent approach satisfying Gauss' law.

The quest for more sophisticated tools utilizing plasma kinetic processes for first-principles simulations is being pursued on several fronts by various groups of researchers. The problem requires self-consistent solution of multi-dimensional multi-fluid equations, which implicitly couple the Maxwell and Navier-Stokes equations and incorporate various inter-molecular and electronic phenomena. Although the difficulty is evident, progress has been reported by various groups. Early efforts are reported by Boeuf et al[17] who developed a model for reactors. Aerospace related analyses solving variants of the mass and momentum equations in the drift-diffusion regime together with a Poisson equation are described by Surzhikov et al,[18] Poggie[19] and Hilbun et al.[20] The research effort of which the present paper forms a part is also attempting to utilize a separate approach developed by Roy et al, who have developed a finite-element approach for RF excited discharges, initially for 1-D phenomena[21] with subsequent extensions reported for 2-D configurations.[22,23] Key attributes of the method are simultaneous treatment of events in both the fluid as well as the dielectric, an integrated approach to coupling the Poisson equation and versatile methods of specifying boundary conditions.

The present effort explores the sensitivity of the flow past a low-speed stalled NACA 0015 wing section to body forces of plasma origin. Since the flow is transitional, a high-fidelity 3-D direct numerical simulation procedure is utilized with dense spatio-temporal resolution to capture the breakdown process. The sensitivity of the flow field is then examined under the impact of body forces of various magnitudes and orientation. The response arising from the complex interaction between the force, non-linear terms and the pressure gradient, is characterized in terms of separation control effectiveness.

II.   Governing equations – Fluid dynamics

The fluid dynamics is assumed to be described by the full Navier-Stokes equations, augmented by terms representing the local forcing of the DBD device. In non-dimensional form, the mass, momentum and energy equations are:

$$\frac{\partial \rho^*}{\partial t^*} + \nabla^* \cdot \left(\rho^* \vec{U}^* \right) = 0 \tag{1}$$

$$\frac{\partial \rho^* \vec{U}^*}{\partial t^*} + \nabla^* \cdot \left[\rho^* \vec{U}^* \vec{\vec{U}}^* + p^* \bar{\bar{I}} \right] - \frac{1}{Re} \nabla^* \cdot \bar{\bar{\tau}}^* = D_c q^* \vec{E}^* \tag{2}$$

$$\frac{\partial \rho^* e^*}{\partial t^*} + \nabla^* \cdot \left[(\rho^* e + p^*) \vec{U}^* - \frac{1}{Re} \left(\vec{U}^* \cdot \bar{\bar{\tau}}^* \right) - \frac{1}{(\gamma-1) Pr M^2 Re} Q_{ht}^* \right] = \beta D_c q \vec{U} \cdot \vec{E} \tag{3}$$

where the superscript $*$ denotes a non-dimensional quantity. $\vec{U}^* = \{u^*, v^*, w^*\}$ is the velocity vector, ρ^* is the density, p^* is the pressure, t^* is time, $\bar{\bar{\tau}}$ is the shear stress tensor, Q_{ht}^* is the heat conduction term, e^* is the total energy, q_c^* is the charge density and $\vec{E}^* = \left\{ E_x^*, E_y^*, E_z^* \right\}$ is the electric field vector. The manner in which the distributions of charge density and the electric field vector are obtained is described later. β, which is either 0 or 1, is a parameter employed to explore the impact of work done by the force. The non-dimensionalization is accomplished through the

following relations:

$$t^* = \frac{tU_{ref}}{L} \quad \rho^* = \frac{\rho}{\rho_{ref}} \quad U^* = \frac{U}{U_{ref}} \quad p^* = \frac{p}{\rho_{ref}U_{ref}^2} \quad \mu^* = \frac{\mu}{\mu_{ref}} \quad T^* = \frac{T}{T_{ref}} \tag{4}$$

where the subscript ref denotes reference values. Several non-dimensional parameters appear, including the Reynolds number $Re = \frac{\rho_{ref}U_{ref}L_{ref}}{\mu_{ref}}$, the Prandtl number $Pr = \frac{\mu_{ref}C_p}{k_{ref}} = 0.72$ and the Mach number $M = \frac{U_{ref}}{\sqrt{\frac{\gamma p_{ref}}{\rho_{ref}}}}$. The molecular viscosity, μ is obtained from Sutherland's law and a perfect gas is assumed.

The parameter D_c, represents the scaling of the electrical to inertial forces is given by:

$$D_c = \frac{\rho_{c,ref}e_c E_{ref}L_{ref}}{\rho_{ref}U_{ref}^2} \tag{5}$$

where ρ_c is the charge number density and e_c is the electronic charge. In the subsequent discussion, the superscript (*) will be dropped and all quantities will be assumed to be non-dimensional unless otherwise explicitly stated.

The governing equations may be written in flux vector form as:

$$\frac{\partial X}{\partial t} + \frac{\partial F_I}{\partial x} + \frac{\partial G_I}{\partial y} + \frac{\partial H_I}{\partial z} = \frac{\partial F_V}{\partial x} + \frac{\partial G_V}{\partial y} + \frac{\partial H_V}{\partial z} + S \tag{6}$$

where X is the solution vector, $X = \{\rho, \rho u, \rho v, \rho w, \rho e\}$, F_I, G_I, and H_I contain terms relevant to inviscid, perfectly conducting media while F_V, G_V, and H_V include effects due to viscosity. For example, F_I and F_V are:

$$F_I = \left\{ \begin{array}{c} \rho u \\ \rho u^2 + p \\ \rho uv \\ \rho uw \\ (\rho e + p)u \end{array} \right\} \tag{7}$$

$$F_V = \left\{ \begin{array}{c} 0 \\ \frac{1}{Re}\tau_{xx} \\ \frac{1}{Re}\tau_{xy} \\ \frac{1}{Re}\tau_{xz} \\ \frac{1}{Re}(u\tau_{xx} + v\tau_{xy} + w\tau_{xz}) + \frac{1}{(\gamma-1)PrM^2Re}\frac{\partial T}{\partial x} \end{array} \right\} \tag{8}$$

The source vector, S contains the terms pertinent to the DBD forcing and are derived either from phenomenological or first-principles models. In order to treat physically complex domains, the above governing equations are extended to curvilinear coordinates in the standard manner[24] by introducing the transformation $x = x(\xi, \eta, \zeta)$, $y = y(\xi, \eta, \zeta)$, $z = z(\xi, \eta, \zeta)$. The strong conservation form is employed to obtain:

$$\frac{\partial \hat{X}}{\partial t} + \frac{\partial \hat{F}_I}{\partial \xi} + \frac{\partial \hat{G}_I}{\partial \eta} + \frac{\partial \hat{H}_I}{\partial \zeta} = \frac{\partial \hat{F}_V}{\partial \xi} + \frac{\partial \hat{G}_V}{\partial \eta} + \frac{\partial \hat{H}_V}{\partial \zeta} + \hat{S} \tag{9}$$

where, with J represents the Jacobian of the transformation, $\hat{X} = X/J$, $\hat{S} = S/J$ and,

$$\begin{aligned} \hat{F}_I &= \frac{1}{J}(\xi_x F_I + \xi_y G_I + \xi_z H_I) \\ \hat{F}_V &= \frac{1}{J}(\xi_x F_V + \xi_y G_V + \xi_z H_V) \end{aligned}$$

with similar expressions for the remaining flux vectors.

III. Numerical Procedure

A high-order compact-difference method is employed to solve the governing equations. Derivatives, phi', of each required quantity, ϕ, are obtained in the uniformly discretized transformed plane (ξ, η, ζ) with the formula:

$$\Gamma\phi'_{i-1} + \phi'_i + \Gamma\phi'_{i+1} = b\frac{\phi_{i+2} - \phi_{i-2}}{4} + a\frac{\phi_{i+1} - \phi_{i-1}}{2} \tag{10}$$

where Γ, a and b determine the spatial properties of the algorithm. All simulations described in this work employ the sixth-order *C6* method, for which $\Gamma = 1/3$, $a = 14/9$ and $b = 1/9$. Details of the spectral characteristics of these schemes, and others obtainable from Eqn. 10, may be found in Refs. 25, 26.

The derivatives of the inviscid fluxes are obtained by first forming these fluxes at the nodes and subsequently differentiating each component. To form terms containing the molecular viscosity μ, the primitive variables u, v, w, T are first differentiated to form the requisite combinations of first derivative terms. These gradients are then differentiated again. In order to reduce the error on stretched meshes, the required metrics are computed in the same manner as the fluxes.[26] An extensive discussion of the metric evaluation procedures for higher-order techniques may be found in Ref. 27.

Additional components are required in the method to enforce numerical stability, which can be compromised by mesh stretching, boundary condition implementation and non-linear phenomena. Spurious frequencies in the solution are systematically removed with a filter designed using spectral analysis. For any component of the conserved vector, ϕ,:

$$\alpha_f \hat{\phi}_{i-1} + \hat{\phi}_i + \alpha_f \hat{\phi}_{i+1} = \Sigma_{n=0}^{N} \frac{a_n}{2} \left(\phi_{i+n} + \phi_{i-n} \right) \tag{11}$$

where $\hat{\phi}$ is the filtered value. The $N + 2$ unknowns, $\alpha_f, a_0, a_1, \ldots a_N$, are derived from Fourier and Taylor-series analyses and determine the order of accuracy and spectral characteristics of the filter. The free parameter α_f, $-0.5 < \alpha_f < 0.5$, is employed to control numerical instabilities. For each α_f within the above bounds, the odd-even mode is completely suppressed and as α_f is reduced, a wider range of frequencies is partially suppressed as described in Ref. 26. The solutions reported in this paper utilize a minimum eighth-order filter with $\alpha_f = 0.2$. Boundary filter expressions have also been derived, both for physical boundaries as well as for artificial interfaces arising from domain decomposition techniques. These formulas and relevant spectral analyses may be found in Ref. 28.

IV.   Results

The problem considered is the flow past a NACA 0015 airfoil at $15 \deg$ angle of attack and a Reynolds number of $45,000$ (see Fig. 1a). All simulations are assumed to be compressible, with the Mach number set at 0.1. In order to capture the breakdown process of the stalled flow at this Reynolds number, a three-dimensional domain is considered, with a spanwise extent of $0.2c$

A.   Mesh resolution and boundary conditions

As noted earlier, the baseline flow is transitional, and even with the high order scheme, requires a relatively large grid. A O-type mesh is employed, comprised of $308 \times 75 \times 145$ points in the x (streamwise), y (spanwise) and z (body-normal) directions respectively. The grid is generated by stacking planes in the manner shown in Fig. 1b. A view of each section is shown in Fig.1c, with an enlarged view in Fig. 1d. The mesh is stretched rapidly in the far-field towards the outer boundary, which is located $30c$ from the surface of the airfoil. The boundary conditions are straightforward. No-slip, zero body-normal pressure-gradient and isothermal wall conditions are enforced at the solid-wall. The far field is assumed to be far enough away for free-stream conditions to be valid while periodic conditions are applied in the spanwise direction as well as at the branch cut arising due to the O-type mesh.

B.   Baseline flow - no control

In order to set the framework for discussion, the baseline case without flow control is described first. As noted earlier, the separated flow field has a complex structure and is unsteady as is the nature of transitional flows. Figure 2a exhibits instantaneous vorticity magnitude iso-levels colored by the spanwise component of vorticity. The breakdown of the shear layer very shortly after separation is clearly evident, generating smaller structures through the development of spanwise instabilities. Although the process is highly three-dimensional, and requires a direct numerical simulation for complete representation, in order to describe the flow succinctly, instantanous quantities will be plotted in spanwise central plane. Figures 2b and c show the instantaneous u velocity and the vorticity magnitude. The shear layer emanates from the separation point, which occurs at approximately 2% chord and the flow may be considered to be fully stalled. Proceeding downstream, the layer loses its coherence as the three-dimensional break-up process progresses. The flow beneath the shear layer is transitional, and is characterized by very low velocities.

Aspects of the unsteady pressure distribution are presented in Fig. 3. Instantaneous contours, Fig. 3a show relatively smooth behavior near the leading edge, but the spanwise instabilities yield coherent structures which propagate downstream. The variation of the pressure in time is indicated in Fig. 3b, which plots the pressure coefficient C_p at
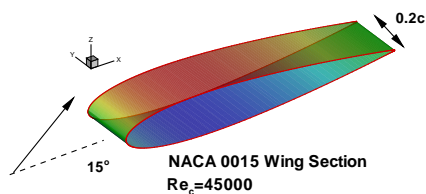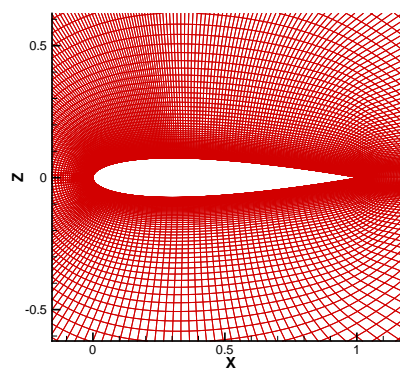
a) Problem simulated
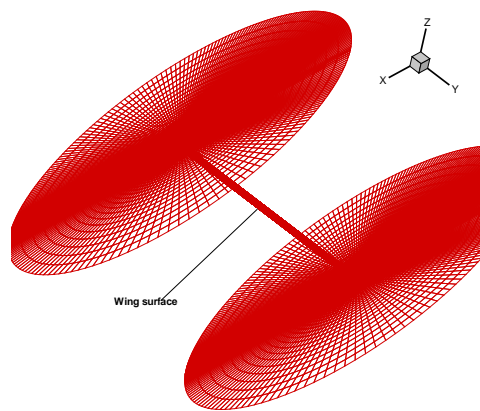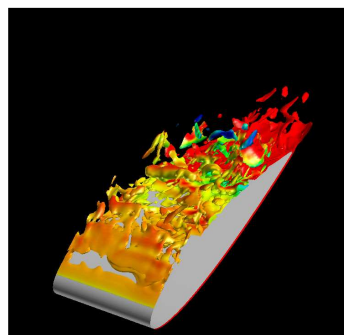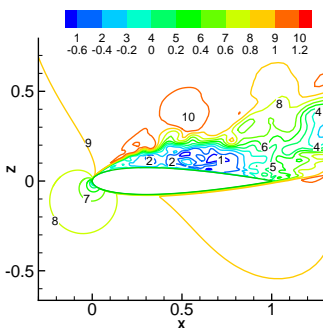

b) Overview of grid structure
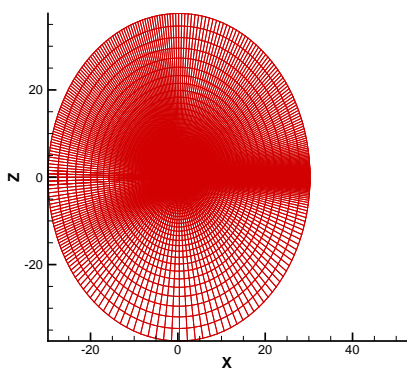
c) Sectional view
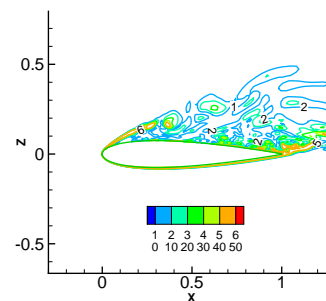

d) Enlarged view

Figure 1. Grid structure

a) 3-D structure - isolevs

b) u-velocity (mid-span)

c) vorticity magnitude (mid-span)

Figure 2. Aspects of instantaneous flowfield without control

the leading and trailing edges. The former location lies upstream of separation and subsequent breakdown of the shear layer, and pressure undulations are observed to be of relatively low frequency. On the trailing edge however, pressure fluctuations are considerably larger, with higher frequency content, and significant negative excursions are evident. Distributions of surface pressure on the airfoil at various points in the time history are plotted in Fig. 3c, together with the mean, which is shown as a solid line. The spatial profiles are smooth on the windward surface, where the flow is attached, but significant deviations are evident on the upper surface, where the flow is highly unsteady.

The mean flow is obtained by averaging the instantaneous solutions over several characteristic times. The structure of the mean flow field is shown in Fig. 4, with contours of the u-velocity, vorticity and the coefficient of pressure, C_p. The separated flow structure is clearly visible. Mean velocities exceed the freestream value at the outer edge of the shear layer by up to $0.2U_\infty$. Significant reversed flow, with velocities reaching up to $-0.6U_\infty$ are evident in the recirculating zones underneath. Figure 4b exhibits ω_y, the spanwise and predominant component of vorticity. The

a) Pressure, C_p | **b)** C_p at L.E and T.E | **c)** Profiles at points in cycle
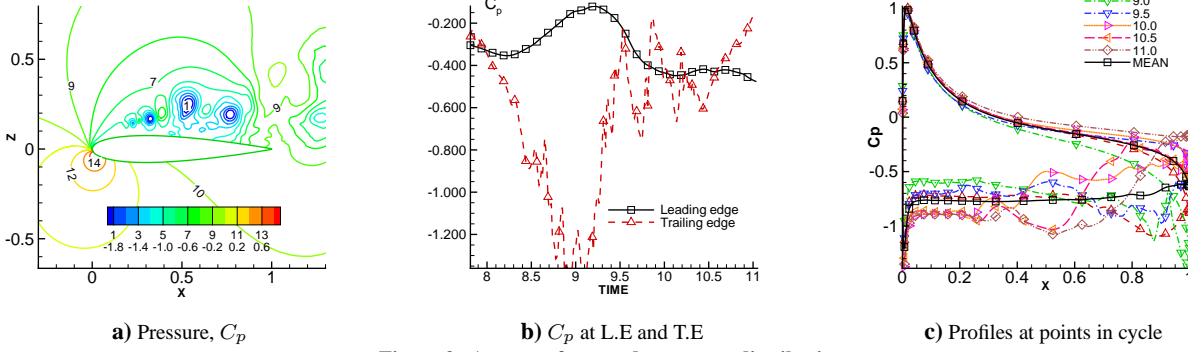
Figure 3. Aspects of unsteady pressure distribution

principal coherent features are those associated with the shear layers emanating from the leading and trailing edges, which exhibit positive and negative values respectively. The fluctuations associated with the features obtained in the breakdown process beneath the separated shear layer (Fig.2a) are averaged out. The pressure contours, Fig. 4c show a large region of low pressure on the upper surface. Lift and drag coefficients of the mean viscous solution are computed to be 0.71 and 0.23, and will be employed to normalize subsequent values. The absence of a spanwise breakdown mechanism in an equivalent 2-D computation at the same flow parameters yields vastly different instantaneous and mean patterns, whose description is deferred to § J.
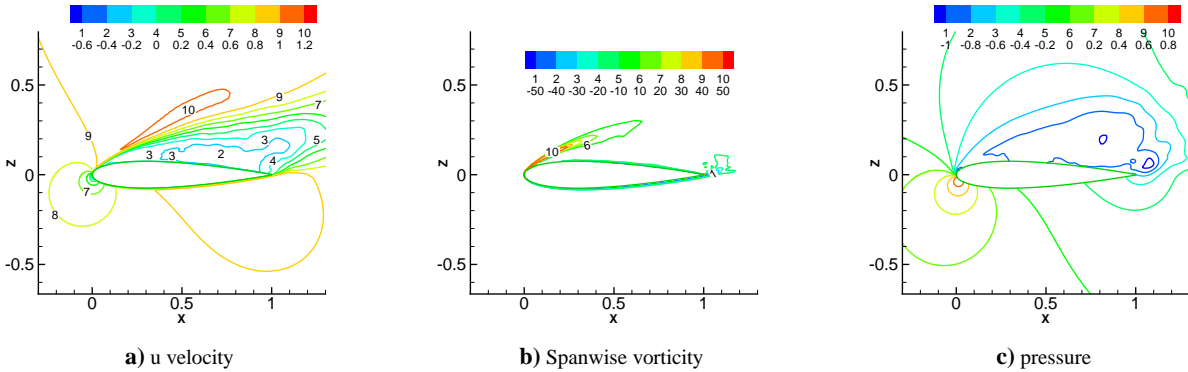

a) u velocity | **b)** Spanwise vorticity | **c)** pressure

Figure 4. Mean structure of 3-D flowfield without control

C. Body force specification

The body force is effectively established by specifying both the charge distribution and the spatial variation of the electric field, from which the Lorentz force is readily deduced. The general development follows that described by Shyy *et al.*[15] However, to factor uncertainties in the model, and to explore the sensitivity of the fully separated flow to different force distributions, additional parameters are introduced to permit variations in actuator orientation, strength and spatial extent. Although the approach is empirical, it provides an attractive framework for a parametric study, greatly facilitating exploratory studies of plasma flow control effectiveness.

The force is obtained from the relation

$$\vec{F} = D_c \theta \Delta t \alpha \rho_c \vec{E} \delta \tag{12}$$

where θ is the frequency of the applied voltage, δt is an effective duty cycle to recover an effective mean force, α is a factor for collision efficiency, ρ_c is the charge density and $\vec{E}$ is the electric field vector. The charge density is assumed to be uniform in the region of interest. The variation in electric field is approximated through several assumptions. The magnitude is assumed to vary linearly in x and y, $|E| = E_o + k_1 x + k_2 y$. Thus, it diminishes from peak value ($= V/d$, where V is the applied voltage and d is the streamwise distance between the two electrodes) at the origin to zero beyond a specified distance from the wall. A further assumption, that the field value is at or above breakdown level in the plasma region, is made to evaluate k_1 and k_2, and to determine the spatial extent of the force distribution. This constraint yields the quantity δ which is 1 when the field is above critical, and zero otherwise. In the frame of reference of the device, $\vec{E}$ is then obtained from:

$$\vec{E} = \frac{|E|}{\sqrt{k_1^2 + k_2^2}} \left\{ \kappa_\xi k_2 \hat{\xi} + \kappa_\eta k_1 \hat{\eta} \right\} \tag{13}$$

a) Force location near leading-edge   **b)** Enlarged view   **c)** Force location near trailing-edge
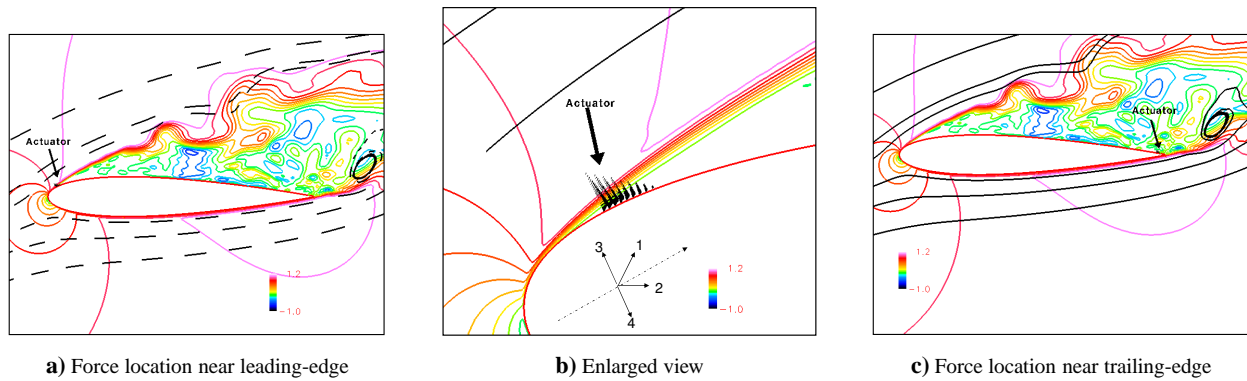
Figure 5. Body force field configurations for phenomenological approach

Here, $\hat{\xi}$ and $\hat{\eta}$ are unit vectors respectively along and normal to the exposed electrode, which is assumed to lie flush on the surface of the body. For the airfoil, this coordinate system is located at the tangent to the surface at the leading edge of the electrode. The orientation is adjusted by choosing κ_ξ and κ_η. In all cases, a single DBD device is assumed, though its location and strength are varied. Four orientations are considered, corresponding to κ_ξ, κ_η pairs of Case 1: $\{1, 1\}$ (the original formulation of Shyy *et al*[15]), Case 2: $\{1, -1\}$ (vertical force component reversed so it points towards the surface), Case 3: $\{0, 1\}$ (normal to body and away from it), and Case 4: $\{0, -1\}$ (normal to body and towards it. Unless otherwise noted, the force is applied at $X = 2.8\%c$, *i.e.,* slightly downstream of the initiation of separation. The values of $\theta = 3000$, $\Delta t = 67\mu s$, $\alpha = 1$, $\rho_c = 10^{11}$ are taken from Ref. 15. The nominal values chosen for the parameters describing strength and extent are $D_c = 2400$, $a = 0.018$ are $b = 0.024$, where a and b are normalized by chord length. The effect of these parameters on the solution is described in § H. Note that for a given plasma parameters such as D_c and θ, the force magnitude is a function of κ_ξ and κ_η. As an example, the force obtained for Case 1, $\{1, 1\}$ is shown in Fig. 5a and b, which superposes force vectors over pressure contours and instantaneous streamlines of the no-control case. One case was also examined with the actuator placed near the trailing edge, Fig. 5c, results for which are described in § G. The force vector is oriented to be generally tangential to the surface, and displays large magnitude near the wall, gradually diminishing to zero in a triangular manner away from the surface, similar to observation of the glow in the experiment. In the present work, as a first step, the force was assumed to be a steady average, and no duty cycle was imposed.

D. Impact of body force on asymptotic response

Figures 6, 7 and 8 exhibit the impact of the each force distribution on instantaneous streamwise velocity, vorticity magnitude and pressure after the solution has been marched to an asymptotic state. The results obtained with Cases 1 and 2 indicate that separation is substantially eliminated. The flow becomes nearly steady, but modest low frequency oscillations are observed in the wake downstream of the trailing edge. In this region, the mesh is relatively coarse, and potential instabilities in the wake may be constrained by the finiteness of the spanwise extent of the domain. Cases 3 and 4 do not yield quasi-steady asymptotes. The ineffectiveness of Case 3, in which the force is pointed normal to and away from the body is not unanticipated, since a parallel may be drawn to the case of wall-normal blowing. When the force is directed vertically downward, the size of the disturbed region above the region is diminished (compare Fig. 6c with 2b), but the solution remains unsteady as coherent structures are triggered and then convected downstream. Although as noted earlier, the magnitude of the force was not normalized in the various cases, the magnitudes of peak velocities provide an indication of the strength and effectiveness of the force distribution. For cases with a streamwise component of force, localized peak velocity magnitudes exceed 3 times that of the freestream. On the other hand, vertical upward force has relatively little impact on peak velocity, while values of about 2.5 are observed for Case 4.

Vorticity magnitude contours for Cases 1 and 2, , Figs. 7a and b indicate an ordered near wall layer on the upper side of the airfoil. Vorticity values are higher, and the layer is thicker, than the boundary layer developing on the windward side. The shear layer leaves the surface slightly upstream of the trailing edge. The detachment angle relative to the freestream is smaller for Case 1 than for Case 2, for which the shear layer detaches along a nearly horizontal line aligning with the freestream only after several chord lengths downstream. In Case 4, which is characterized by a shallow separation region and unsteady boundary layer development, peak values of vorticity are rapidly damped on proceeding downstream of the body force. The absence of a coherent wall-jet (except in initial transients) in this simulation inhibits the generation of vorticity near the wall through the viscous mechanism. Similar conclusions on the overall flowfield may be drawn from pressure contours for Cases 1, 2 and 4 depicted in Fig. 8a through c (Case 3 is not shown because of the ineffectiveness of this force configuration). In contrast to the baseline simulation (Fig.3a), each
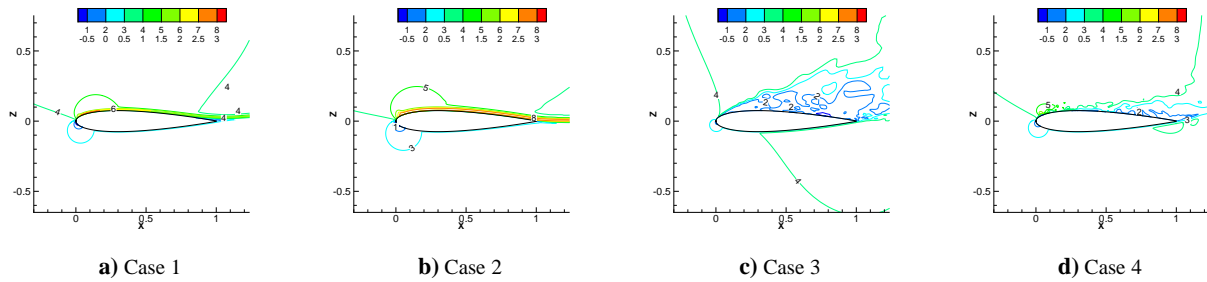
a) Case 1   **b)** Case 2   **c)** Case 3   **d)** Case 4

Figure 6. Instantaneous u-velocity contours obtained with different force configurations

of these controlled flows displays a strong suction peak near the point of application of the force. Figure 8d exhibits C_p on the surface for all four cases with control. For Cases 3 and 4, which remain highly unsteady, a representative instantaneous value has been plotted. Lowest pressures on the upper surface ($C_p < 0$) are observed with Cases 1 and 2. Both Cases 2 and 4, which have a significant component of body force towards the wall also show a sharp local peak in pressure where the force is applied. Comparison with the mean flow results of Fig.3c indicate that flow attachment observed for Cases 1 and 2 are accompanied by reduction in the suction surface pressure, and thus an increase in lift coefficient. Representative values are 2.3 and 2.8 respectively (normalized by values obtained for the baseline case). Analysis shows that for these two cases, thrust is also generated, consistent with a jet velocity profile in the wake of the airfoil, as discussed below. Case 4 with the body force directed towards the wall continues to exhibit drag but it is far smaller than that obtained without control.
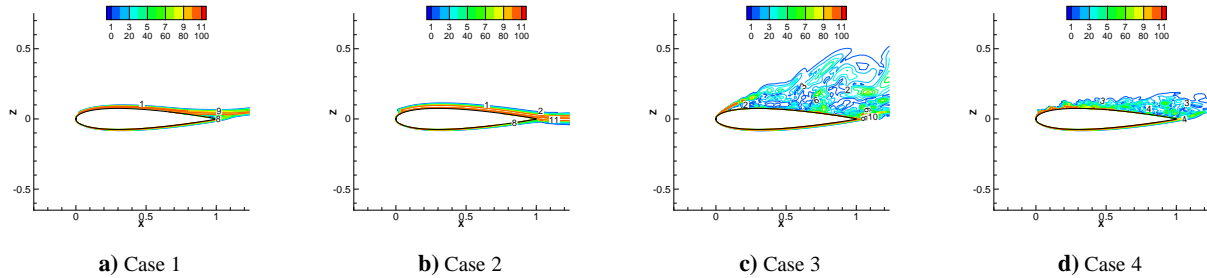

a) Case 1   **b)** Case 2   **c)** Case 3   **d)** Case 4

Figure 7. Instantaneous contours of vorticity magnitude obtained with different body force configurations

a) Case 1   **b)** Case 2   **c)** Case 4   **d)** Surface pressure
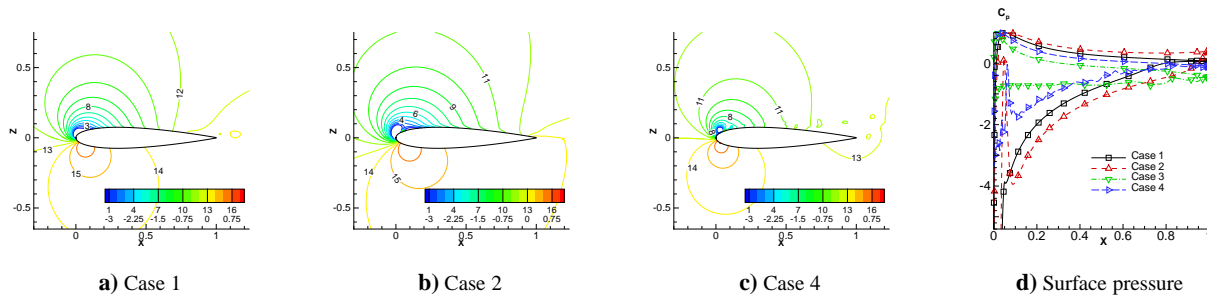
Figure 8. Instantaneous pressure contours obtained with different force configurations

Instantaneous velocity profiles at mid-chord and mid-span of the upper surface are shown in Fig. 9a. Both Case1 and Case 2 depict the anticipated development of a wall jet (see Ref. 11) extending about $0.1c$ above the wall. In contrast, the no-control and Case 3 perturbation both exhibit negative velocities in the separated region, while the effect of a purely downward force, Case 4, yields somewhat smaller reversed flow region. Mid-chord profiles of the spanwise component of vorticity are depicted in Fig. 9b. The no-control mean profile indicates a negative component, since the mean flow is separated at this location. Both Cases 1 and 2, for which the solution is relatively steady, show positive values very near the wall, but also exhibit a reversal of vorticity in the region beyond $z \sim 0.07$. The reversal reflects the wall-jet nature of the near wall flow. In the interior of the region of applied force, the curl of the distribution, Fig. 5, possesses a negative spanwise component, which is overcome by the viscous stresses generated near the wall because of the no-slip condition and the required balance with the pressure gradient.
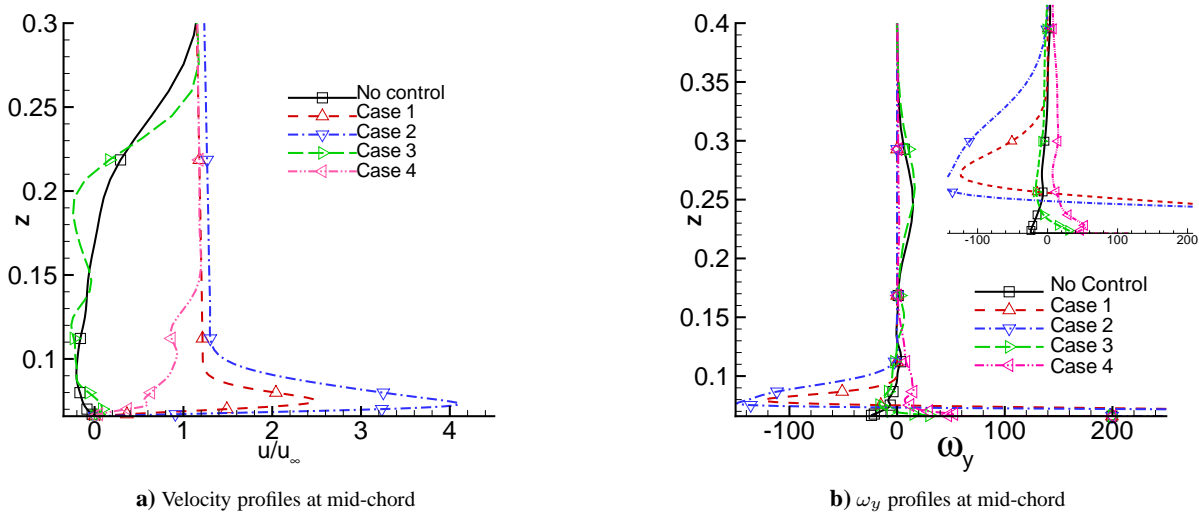
a) Velocity profiles at mid-chord   **b)** ω_y profiles at mid-chord

Figure 9. Effect of control on flow field surveys

E.   Transient response following control onset

The transient process by which flow control is established is shown in Fig. 10 for Case 2 using u-velocity. The wall jet structure is initiated at the point of application of the force. The front propagates downstream in a relatively monotonic fashion until the flow is completely attached, which occurs at about $0.85T_c$, where $T_c = c/U_\infty$ is the characteristic time. The fluctuations diminish while the flow on the lower surface remains relatively unaffected by the control. When the quasi-steady state is reached, the shear layer formed in the wake by the merging of flows from the lower and upper surfaces retains its jet like structure for a significant distance downstream of the trailing edge. The peak velocity, whose value near the trailing edge is about 3.5, decreases to about 3 and 2 one and two chords downstream.

The characteristic time with which the flow responds to the body force depends on the nature of the force with Case 2 displaying slightly shorter transients than Case 1. The latter case in fact exhibits a more pronounced impulse effect where the flow first attaches to the surface and remains so for nearly 2 characteristic times. A representative flow field for this case, at $t = 2T_C$ is shown in Fig. 10g. During this period, lift and drag values remain relatively stable, but a mild unsteadiness is observed in the wake shear layer region. A small reversed flow bubble attached to the trailing edge persists, as shown in Fig. 10h. A similar region exists for Case 2 as shown, but the orientation of this bubble is parallel to the upper surface, while it is more horizontal for Case 1. Subsequently, for Case 1, the bubble increases in size in a very gradual fashion, and separation moves upstream – in the final solution plotted in Fig.6a, separation is located at $x \sim 0.8c$.
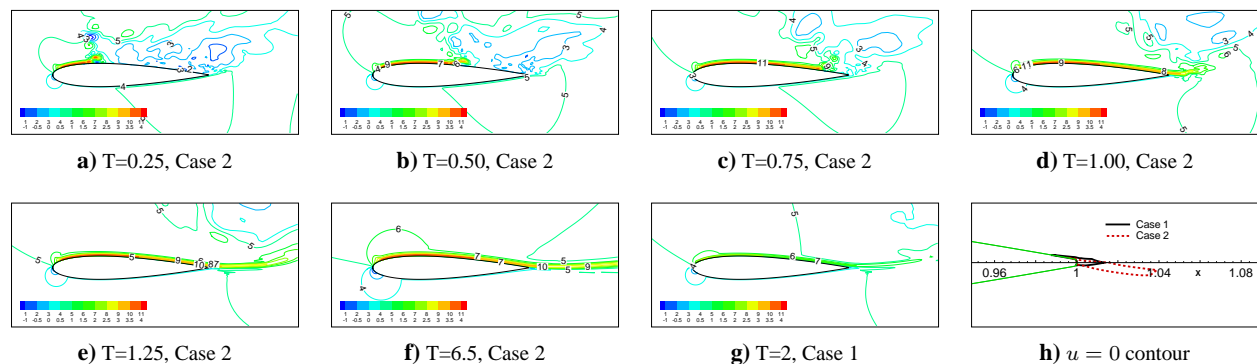

a) T=0.25, Case 2   **b)** T=0.50, Case 2   **c)** T=0.75, Case 2   **d)** T=1.00, Case 2

e) T=1.25, Case 2   **f)** T=6.5, Case 2   **g)** T=2, Case 1   **h)** $u = 0$ contour

Figure 10. Evolution of flowfield after control is switched on. Frames a through f are u-velocity contours for Case 2, frame g is for Case 1.

F.   Transient response following control cessation

Further insight into relaxation timescales is derived by examining the response of the flow when the force is abruptly switched off after the asymptotic state was reached: this simulation is denoted Case 5. Results are shown in Fig. 11 in terms of u-velocity contours at various time instants, designated in terms of characteristic times, measured subsequent to the switch-off. Immediately following control switch-off, the overshoot characteristic of the wall-jet due to lack of

body-force ceases and this effect is observed to progress downstream In the immediate aftermath of the switch-off, a thinning process is observed to propagate through the upper boundary layer in time with a convective speed. This progression moves downstream at a phase velocity corresponding to a non-dimensional velocity of about 1.6, reaching the trailing edge after about $0.6T_c$, where T_c is the characteristic time. At about $0.7T_c$, indications of flow separation are evident near the leading edge. This unsteady separation phenomenon is characterized by the onset of reversed flow and formation of vortices similar to those observed in the initiation of dynamic stall. Figure 11i exhibits velocity contours after a several characteristic times and indicates that the solution features resemble the no-control state. Thus, in this case, no tendency towards hysteresis is observed.

Figure 11j exhibits surface pressures (p/p_∞) at various time instants. The initial indication of body force cessation manifests first in the pressure field as a clearly discernable rise near the actuator location in less than 0.01 characteristic time. Profiles of static pressure at the leading edge, mid-chord (suction surface) and trailing edge are shown in Fig. 11k. Near the leading edge, the pressure increases after the force is removed. At mid-chord and near the trailing edge, major oscillations are observed after $0.3T_c$ at mid chord and about $1T_c$ respectively, indicating a reduction in phase velocity as the initial perturbation progresses downstream.
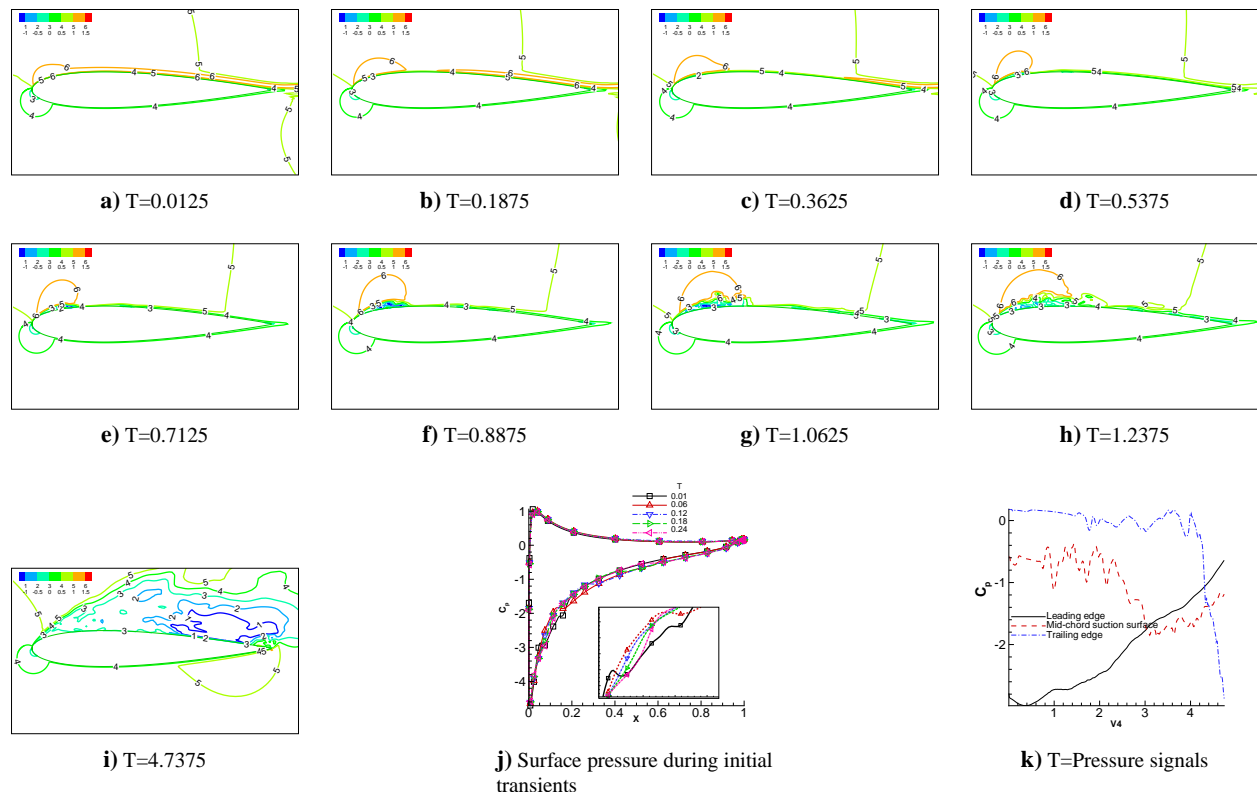

a) T=0.0125

b) T=0.1875

c) T=0.3625

d) T=0.5375

e) T=0.7125

f) T=0.8875

g) T=1.0625

h) T=1.2375

i) T=4.7375

j) Surface pressure during initial transients

k) T=Pressure signals

Figure 11. Case 5: Evolution of flow field after body force is turned off

G. Effect of locating actuator near trailing edge

The effect of placing the device at the trailing edge, as in Fig. 5c, is shown in Fig. 12, which shows results about $3T_c$ after initiation of the force. It is evident that the flow near the leading edge, in the vicinity of the separating shear layer is not significantly influenced in a manner indicating attachment (see *e.g.,* Fig. 2b). However, near the trailing edge, the initiation of a large scale event comprised of a trailing vortex system is evident. Instantaneous pressure traces at the leading, mid-chord and trailing edges are depicted in Fig. 12d. Although the simulation was halted before an asymptotic state was reached, the figures indicate clearly the localized nature of the effect.

H. Effect of actuator strength and scale

The effect of force strength and scale is explored by halving the size of the device (a and b) and the strength (D_c) compared to those of Case 1. Features of the flow after an asymptotic state is reached are exhibited in Fig. 13 in terms of instantaneous velocity, vorticity magnitude and pressure. It is evident that although the massive separation region observed in Fig. 3 is considerably diminished and the shear layer is at a smaller incline to the surface of the
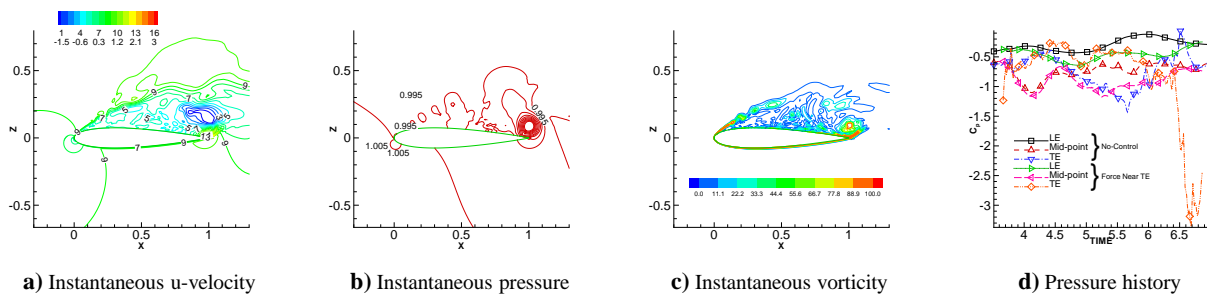
a) Instantaneous u-velocity **b)** Instantaneous pressure **c)** Instantaneous vorticity **d)** Pressure history

Figure 12. Effect of actuator near trailing edge

airfoil. However, the wall-jet layer experiences unsteady separation a short distance downstream of the point of force application. Pressure contours show that an adverse gradient is encountered at this point. Peak values of velocity are much lower with the smaller forcing. Vorticity is also not confined to a thin region as with Case 1 (Fig.7a) but rather exhibits an unsteady three-dimensional distribution characteristic of a shear layer instability.
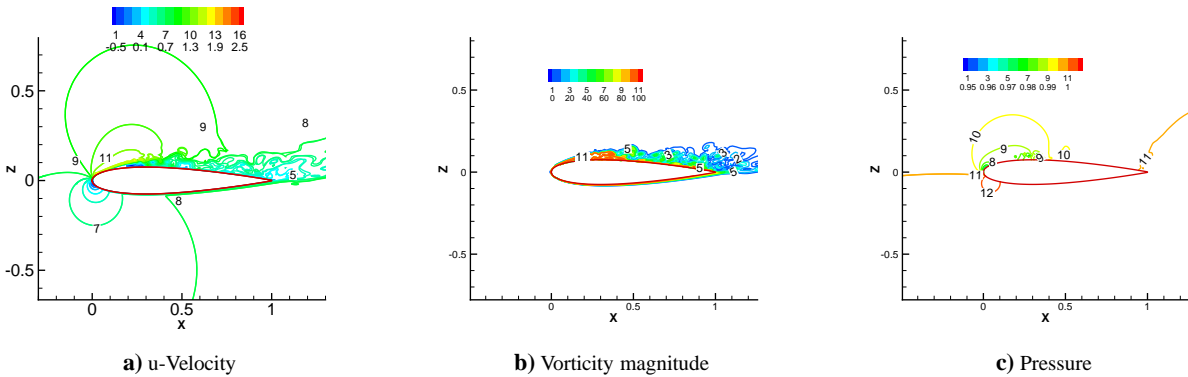

a) u-Velocity **b)** Vorticity magnitude **c)** Pressure

Figure 13. Effect of force strength and scale

I.   Impact of work done by body force

The impact of work done by the force was also explored for Case 1 by setting $\beta = 1$, thus adding the term $D_c q^* \vec{U} \cdot \vec{E}^*$ to the energy equation (see Eq. 3). Results are compared in Fig. 14a and b with simulations in which the work term is not considerd. Figure 14a, which depicts u-velocity contours indicates that there is no qualitative difference in the obtained flow structure. The prominent wall-jet on the upper surface has similar properties in terms of peak velocities and downstream development. Figure 14b, in which surface pressure is plotted for the two cases, shows that quantitative effects of the work term on pressure are also minor. Figure 14c, showing density contours when the work term is on, indicates that the maximum density change near the point of application is limited to about 2%. Clearly compressibility effects are not necessary for effective control. The Mach number in this case directly reflects the increase in velocity.
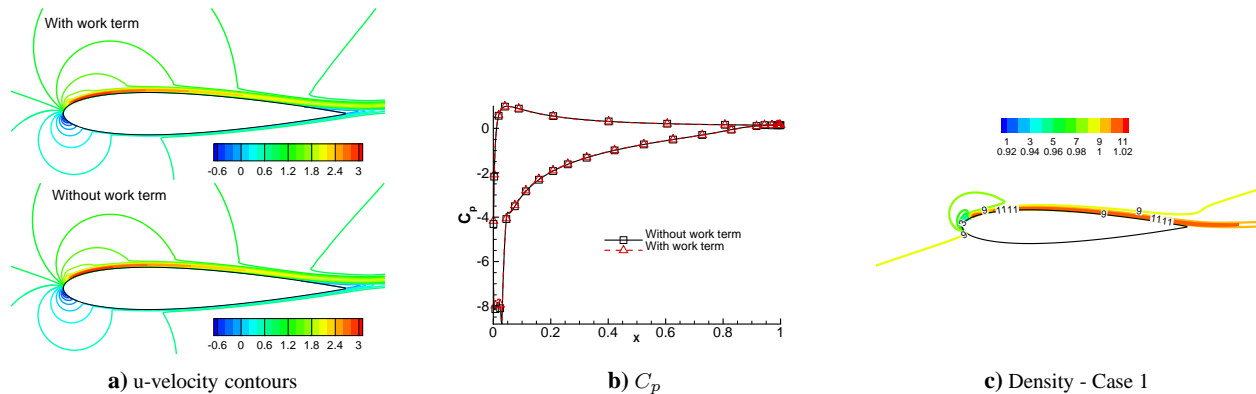

a) u-velocity contours **b)** C_p **c)** Density - Case 1

Figure 14. Effect of work term in governing equations

J. 2-D Simulations

The absence of a spanwise breakdown mechanism in a 2-D computation at the same flow parameters yields a vastly different pattern in both instantaneous and mean flowfields. Contours of select instantaneous and mean quantities are plotted in Fig. 15 for the baseline no-control case. In this case, shed vortices maintain their form in an unphysical fashion, giving rise to a sequence of large structures in the form of vortex pairs that are shed downstream at various intervals. Peak instantaneous velocities, Fig. 15a, are considerably larger, reaching almost twice those observed in the 3-D simulations in localized regions. In a consistent fashion, instantaneous pressure contours exhibit coherent features in which extrema which are much higher than in the full simulation. The mean profile, Fig. 15c, exhibits striking qualitative and quantitative differences from both instantaneous 2-D and mean 3-D counterparts, with a lower incline of the separated shear layer relative to the surface of the airfoil.
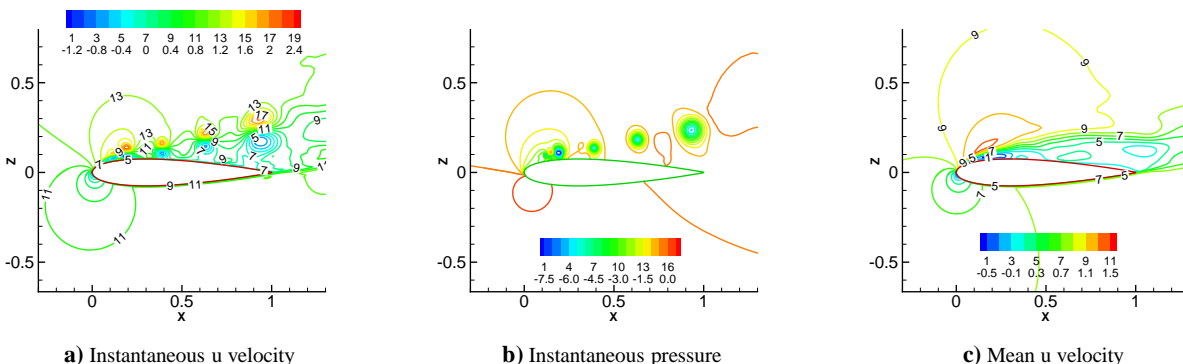

a) Instantaneous u velocity   b) Instantaneous pressure   c) Mean u velocity

Figure 15. Structure obtained with 2-D simulations without control

Pointwise pressures obtained with a 2-D calculation are presented in Fig. 16a, and may be compared with the 3-D results of Fig. 3b. In this case, leading edge pressure profiles are generally lower than at the trailing edge, in contrast to the 3-D situation, and the impact of the relatively larger structures of the 2-D simulation is evident. Both traces also exhibit higher frequency content. Lift and drag coefficients, normalized relative to the mean 3-D values, are shown versus time in Fig 16b. The 2-D simulation yields significantly higher lift values and moderately lower drag values than the 3-D case, the combined effect giving rise to a higher C_L/C_D ratio. Mean surface pressure distributions are depicted in Fig. 16c. Whereas the 3-D result shows a relatively flat mean profile on the upper surface as is characteristic of stall, while by contrast, the 2-D results shows a unphysical large region of low pressure under the shed vortex system, consistent with the observed higher lift.
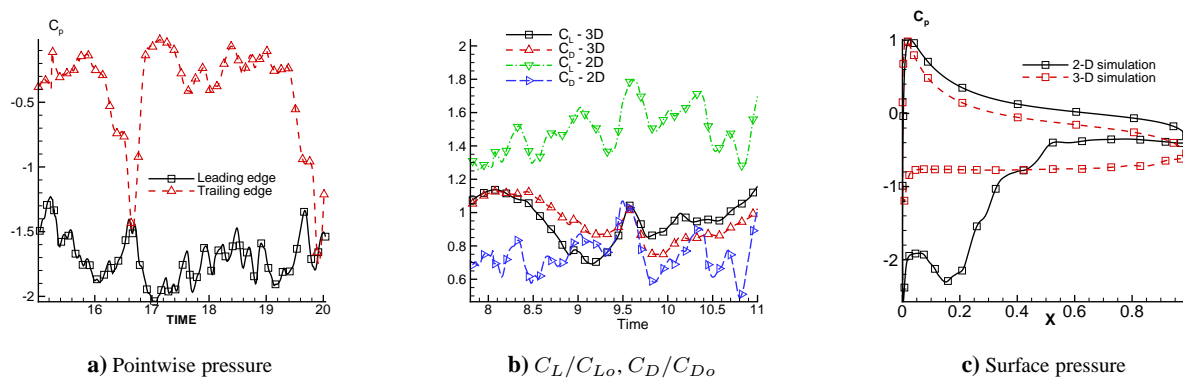

a) Pointwise pressure   b) $C_L/C_{Lo}, C_D/C_{Do}$ c) Surface pressure

Figure 16. Pointwise and surface values of pressure and mean comparison with 3-D results

Several conclusions may be derived from simulations in which the effect of the applied body force is examined on these 2-D solutions. The results suggest that when the attachment process is complete, as in Case 2 above, both approaches yield similar results. This is exhibited in Fig. 17a which shows C_p values from 2-D and 3-D results when an asymptotic state is reached. Indeed, when separation is completely inhibited, the 3-D simulation is essentially 2-D near the airfoil, with negligible computed spanwise velocities in the vicinity of the airfoil, except downstream of the trailing edge. Furthermore, with the exception of mild unsteadiness in the wake, the solution is also fairly steady in the region near the wing.

On the other hand, when the flow is unsteady, different results are obtained from the 2-D and 3-D approaches. Unsteadiness may be associated either with the initial onset of transients after the application or cessation of the force,

or when the asymptotic state itself is unsteady. The former situation is illustrated in Fig. 17b which depicts the state of the flow at $0.25T_c$ following control onset. The attachment front has penetrated further downstream and exhibits more eruptive deviation from the wall in the 2-D case than in the 3-D case. The velocities inside the wall-jet are also seen to be larger in the 2-D case. Some of these variations partly reflect differences in the initial conditions between the two simulations. Nonetheless, these results suggest that simulations seeking to optimize duty cycle considerations, which depend fundamentally on transient response, may require full 3-D analyses. The situation when the asymptotic state is itself unsteady typically arises when reattachment is incomplete. In such situations, a separated shear layer or unsteady boundary layer exists, whose dynamics in 2-D and 3-D are different, in much the same fashion as observed without flow conrol. An example is the low forcing case described above, for which the 3-D simulation exhibits only partial reattachment. Corresponding instantaneous snapshots with the two simulation approaches when an asymptotic state is reached are shown in Fig. 17c. Key differences are evident in the extent of the shear layer before unsteady processes are generated, and the manner in which coherent features appear downstream. Another interesting situation in which 2-D and 3-D simulations differ is observed for Case 1. As shown earlier in Fig.6, in the 3-D simulation separation is observed close to the trailing edge, and yields a relatively stable solution in the region of interest. However, in the corresponding 2-D simulation, an instantaneous pattern of which shown in Fig. 17c (bottom) together with the 3-D pattern (top), the solution is unsteady and is characterized by shedding associated with the complex merging of the wall-jet and the boundary layer from the lower surface of the wing section.
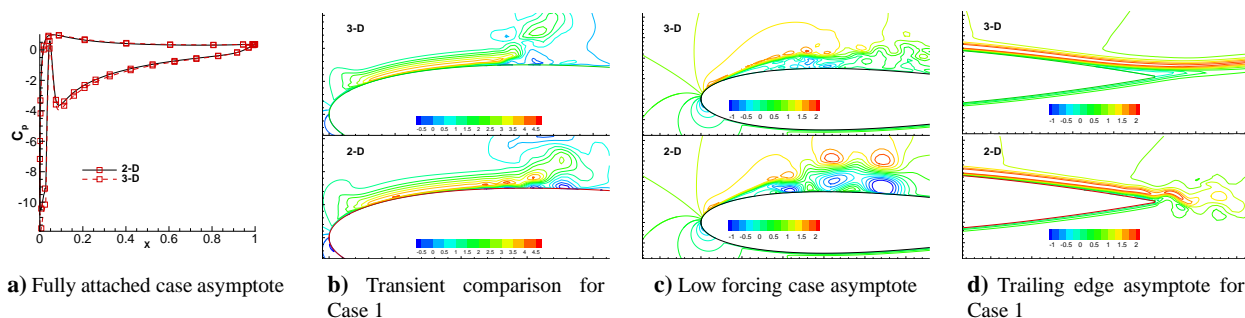

a) Fully attached case asymptote **b)** Transient comparison for Case 1 **c)** Low forcing case asymptote **d)** Trailing edge asymptote for Case 1

Figure 17. Effect of forcing on 2-D simulations

V.   Conclusion

The response of a separated flow field to body forces arising from suitably placed radio frequency dielectric barrier discharge actuator is explored. A separated flow past a NACA 0015 airfoil at $15\,\deg$ angle of attack and Reynolds number $45,000$ is considered. Various force configurations are specified, and the response of the flow field is characterized with 3-D direct numerical simulations utilizing a high-order method comprised of sixth-order compact differencing and 10th order filtering. It is observed that the response of the flowfield is determined by a complex interplay between the properties of the body force, inertial terms and the pressure field. In general, a significant downstream component of the body force is beneficial to reduce stall, and complete elimination is observed at adequate force magnitude even though the spatial extent of actuation is small relative to the size of the chord. Attachment is characterized by the formation of a stable wall-jet on the upper surface. When the only force component is normal and towards the wall, the viscous layer developing downstream is susceptible to instability and asymptotically unsteady flow is obtained. In an effort to characterize the transient response pertinent to duty cycle considerations, relaxation effects are studied by suddenly switching off actuation and tracking the reappearance of separation. The absence of spanwise breakdown of vortices in the 2-D flow simulation results in large coherent structures which respond differently to the applied perturbation. Nonetheless, if and when stall is eliminated, the flowfield becomes generally 2-D, and the overall features of 2-D and 3-D analyses are similar. Several avenues for future work may be identified, including the impact of duty cycles, multiple actuators, scaling effects with Reynolds number and angle of attack as well as more effective coupling approaches with advanced first-principles based simulations.

References

[1] Kolesnichenko, Y. F., Brovkin, V., Azarova, O., Grudnitsky, V., Lashkov, V., and Mashek, I., "Microwave Energy Release Regimes for Drag Reduction in Supersonic Flows," *AIAA Paper 2002-0353*, 2002.

[2] Leonov, S., Kuryachii, A., Yarantsev, D., and Yuriev, A., "Study of Friction and Separation Control by Surface Plasma," *AIAA Paper 2004-0512*, 2004.

[3] Enloe, C., McLaughlin, T., VanDyken, R., Kachner, K., E.J., J., and Corke, T., " ," *AIAA Paper 2003-1021*, Jan 2003.

[4] Roth, J., "Aerodynamic flow acceleration using paraelectric and peristaltic electrohydrodynamic (EHD) effects of a One Atmosphere Uniform Glow Discharge Plasma (OAUGDP)," *Phys. Plasmas*, Vol. 10, 2003, pp. 2117.

[5] Roth, J., Sin, H., R.C.M., M., and Wilkinson, S., "Flow Re-attachment and Acceleration by Paraelectric and Peristaltic Electrohydrodynamic Effects," *AIAA Paper 2003-531*, Jan. 2003.

[6] Post, M. and Corke, T., "Separation Control on High Angle of Attack Airfoil Using Plasma Actuators," *AIAA Paper 2003-1024*, 2003.

[7] Corke, T., Jumper, E., Post, M., Orlov, D., and McLaughlin, T., "Application of Weakly-Ionized Plasmas as Wing Flow-Control Devices," *AIAA Paper 2002-0350*, Jan. 2002.

[8] Post, M. and Corke, T., "Separation Control Using Plasma Actuators - Dynamic Stall Control on an Oscillating Airfoil," *AIAA Paper 2004-2517*, June 2004.

[9] Opaits, D., Roupassov, D., Starikovskaia, S., Starikovskii, A., Zavialov, I., and Saddoughi, S., "Plasma Control of Boundary Layer Using Low-Temperature Non-Equilibrium Plasma of Gas Discharge," *AIAA Paper 2005-1180*, Jan. 2005.

[10] List, J., Byerley, A., McLaughlin, T., and VanDyken, R., "Using Plasma Actuators Flaps to Control Laminar Separation on Turbine Blades in a Linear Cascade," *AIAA Paper 2003-1026*, Jan. 2003.

[11] Jacob, J., Rivir, R., Carter, C., and Estevadeordal, J., "Boundary Layer Flow Control Using AC Discharge Plasma Actuators," *AIAA Paper 2004-2128*, June 2004.

[12] Jacob, J., Ramakumar, K., Anthony, R., and Rivir, R., "Control of Laminar and Turbulent Shear Flows Using Plasma Actuators," *Fourth Int. Symp on Turbulence and Shear Flow Phenomena*, , No. TSFP4-225, June 2005.

[13] Corke, T. and Post, M., "Overview of Plasma Flow Control: Concepts, Optimization and Applications," *AIAA Paper 2005-0563*, 2005.

[14] Baird, C., Enloe, C., McLaughlin, T., and Baughn, J., "Acoustic testing of the dielectric barrier discharge (DBD) plasma actuator," *AIAA Paper 2005-0565*, Jan 2005.

[15] Shyy, W., Jayaraman, B., and Andersson, A., "Modeling of Glow-Discharge Induced Fluid Dynamics," *J. Appl. Phys.*, Vol. 92, 2002, pp. 6434.

[16] Voikov, V., Corke, T., and Haddad, O., "Numerical simulation of flow control over airfoils using plasma actuators," *Bulletin of the APS*, 2004.

[17] Boeuf, J. and Pitchford, L., "Two-Dimensional Model of a Capacitively Coupled RF Discharge and comparisons with experiments in the Gaseous Electronics Conference Reference Reactor," *Phys Ref*, Vol. E 51, 1995, pp. 1376.

[18] Surzhikov, S. and Shang, J., "Multi-Fluid Model of Weakly Ionized Electro-Negative Gas," *AIAA Paper 2004-2659*, June 2004.

[19] Poggie, J., "Numerical Exploration of Flow Control with Glow Discharges," *AIAA Paper 2004-2658*, June 2004.

[20] Hilbun, W. and Case, B., "Preliminary Development of a Computational Model of a Dielectric Barrier Discharge," *AIAA Paper 2005-1176*, Jan 2005.

[21] Roy, S. and Gaitonde, D., "Radio frequency induced ionized collisional flow model for application at atmospheric pressures," *J. Appl Phys*, Vol. 96, 2004, pp. 2476–2481.

[22] Roy, S. and Gaitonde, D., "Modeling Surface Discharge Effects of Atmospheric RF on Gas Flow Control," *AIAA Paper 2005-0160*, Jan 2005.

[23] Roy, S. and Gaitonde, D., "Multidimensional Collisional Dielectric Barrier Discharge for Flow Control at Atmospheric Pressures," *AIAA Paper 2005-4631*, 2005.

[24] Anderson, D., Tannehill, J., and Pletcher, R., *Computational Fluid Mechanics and Heat Transfer*, McGraw-Hill Book Company, 1984.

[25] Lele, S., "Compact Finite Difference Schemes with Spectral-like Resolution," *Journal of Computational Physics*, Vol. 103, 1992, pp. 16–42.

[26] Gaitonde, D., Shang, J., and Young, J., "Practical Aspects of Higher-Order Numerical Schemes for Wave Propagation Phenomena," *Int. Jnl. for Num. Methods in Eng.*, Vol. 45, 1999, pp. 1849–1869.

[27] Visbal, M. and Gaitonde, D., "Very High-Order Spatially Implicit Schemes for Computational Acoustics on Curvilinear Meshes," *J. Comp. Acoustics*, Vol. 9, No. 4, 2001, pp. 1259–1286.

[28] Gaitonde, D. and Visbal, M., "Pade-type Higher-Order Boundary Filters for the Navier-Stokes Equations," *AIAA J.*, Vol. 38, No. 11, Nov. 2000, pp. 2103–2112.